Journal of *Marine Science and Engineering*

MDPI

Article

Uncertainty Assessment of Wave Elevation Field Measurement Using a Depth Camera

Hoyong Kim [1], Chanil Jeon [2], Kiwon Kim [1] and Jeonghwa Seo [1,*]

[1] Department of Naval Architecture and Ocean Engineering, Chungnam National University, Daejeon 34134, Republic of Korea
[2] Department of Health Sciences and Technology, Sungkyunkwan University, Seoul 06355, Republic of Korea
* Correspondence: j.seo@cnu.ac.kr; Tel.: +82-42-821-6628

Abstract: The present study suggests a methodology for acquiring wave elevation fields using a depth camera sensor, with assessment results for the test uncertainty. The depth camera module of an Azure Kinect is calibrated using marker arrays on the optic table, to obtain a polynomial mapping function between the pixel-wise and physical position. For installation of the depth camera in a wave channel, the system is aligned using the built-in inertial measurement unit of Azure Kinect to be perpendicular to the calm water surface. The systematic and random standard uncertainties were evaluated from the analysis of calibration and repeated tests, respectively. The wave height measurement results for the depth camera were compared to those for the capacitance-type and ultrasonic wave height gauges. The test uncertainty of the depth camera increased in large wave stiffness conditions, where the time-of-flight sensor has a disadvantage in measurement.

Keywords: depth camera; wave height gauge; calibration; test uncertainty

check for updates

Citation: Kim, H.; Jeon, C.; Kim, K.; Seo, J. Uncertainty Assessment of Wave Elevation Field Measurement Using a Depth Camera. *J. Mar. Sci. Eng.* **2023**, *11*, 657. https://doi.org/10.3390/jmse11030657

Academic Editor: Christos Tsabaris

Received: 22 February 2023
Revised: 17 March 2023
Accepted: 20 March 2023
Published: 21 March 2023

Copyright: © 2023 by the authors. Licensee MDPI, Basel, Switzerland. This article is an open access article distributed under the terms and conditions of the Creative Commons Attribution (CC BY) license (https://creativecommons.org/licenses/by/4.0/).

1. Introduction

The free-surface wave is one of the most significant research topics in naval architecture and ocean engineering, particularly in fields such as bridge engineering [1–3], offshore wind turbine design [4–6], and offshore platform design [7–10]. To comprehend the physics of behavior at the air–water interface through experiments, quantitative features of the phenomena, i.e., the wave height and period, have been charted using wave height gauges. Towing tank model tests were utilized with wave height gauges to derive the response amplitude operator (RAO) of test models of regular waves [11–13] and analyze energy spectra in irregular waves [14]. In addition, the wave patterns around advancing ship models and structures in waves were measured to investigate the wave–model interactions [15–17].

To measure wave elevation, various types of wave height gauges have been used. A capacitance-type wave height gauge is the most common, owing to its reliability and ease of installation and operation. It is an invasive method, measuring the immersion depth of a vertical wire fixed on the model surface or bracket. Thanks to its easy installation, the system has been applied to measure flooding behavior in a compartment, as well as the elevation of external waves [18–20].

An ultrasonic distance gauge is a non-invasive and inexpensive solution for wave elevation measurement. It simply senses the distance between the probe and the water surface using an ultrasonic time-of-flight (ToF) sensor. The ultrasonic wave height gauge does not disturb the water surface; thus, it has advantages for measuring the wave elevation of high-speed flows where an invasive method suffers vortex-induced vibration of probes [11,13,14,21,22].

A servo-needle-type wave height gauge uses a needle that remains in contact with the water surface, vertically traversed by a servo motor. It swiftly responds to the wave elevation change; thus, it enables precise measurement in rough wave conditions. However,

owing to the size of the servo actuator, the sensor has one drawback, that is, the arrangement is restrained in model tests [15].

The wave height gauges described above are pointwise measurement systems that acquire the time series of the wave elevation at a certain point. To obtain a field of wave elevation, multiple sensors are arranged, or the tests are repeated by changing the location of wave gauges [15,23]. Such a process is quite time consuming; therefore, tests of wave elevation field measurement and wave pattern analysis are quite rare, despite their importance.

To obtain a wave elevation field, optical wave height measurements have been introduced for tests in laboratory conditions [24,25] and observation in the actual sea [26–28]. The optical approaches were reviewed in the studies of van Meerkerk et al. [29] and Gomit et al. [30]. The measurement principle of particle image velocimetry (PIV) and particle tracking velocimetry (PTV) was applied to water surface tracking [31]. The depth detection mechanism of stereoscopic PIV was successfully utilized for the water surface elevation measurement with seeded tracer particles [32,33]. The seeding particle was replaced by a patterned laser projection or reflected image. The projection usually requires dye to reflect the projected pattern at the water surface [34,35]. Instead of the patterned image projection, a laser beam array [36] and a multi-colored pattern [37] were used to estimate the wave elevation from the deformation of the pattern. Jähne et al. [38] imaged wave boundaries by using a light array on the flume bottom. Besides external light sources, the polarization of reflected light on the water surface is an effective approach for wave elevation field measurement. Zappa et al. [39] introduced the polarimetric slope sensing method to both the laboratory and an actual river stream.

Thanks to recent advances in optical sensors, the point cloud, recognizing three-dimensional (3D) geometry as sets of points, has been used in various fields of research [40,41]. If the point cloud is applied to wave elevation measurement, the 3D geometry of the water surface, that is, the wave elevation field, can be ascertained. A depth camera is a common sensor for acquiring point clouds, owing to its advantages of a cheap price and robust hardware structure. In the field of ocean engineering, a depth camera was used for wave elevation measurement in regular waves, and the researchers compared the results with those for a captive-type wave height gauge [42,43]. The measurement enabled temporal and spatial analysis of the wave height field, like the space–time Fourier wave spectrum, to find the dominant energy modes.

Inspired by the study of Toselli et al. [42], the present study aims to assess the test uncertainty of the wave elevation field measurement using a depth camera with calibration. The wave elevation field measurement of the present study is similar to PIV. For studies on test uncertainty assessment of PIV, refer to [44–46]. The calibration method using a calibration target is suggested to correct the spatial distortion of the depth image. The measurement uncertainty is quantified with a variation of the wave stiffness conditions. It is compared with the uncertainty of common pointwise wave height measurement systems, i.e., the capacitance-type and ultrasonic wave height gauges.

This paper is organized as follows. In Section 2, the test setup and apparatus for wave elevation measurement are described. Section 3 provides the principles of test uncertainty assessment. The calibration procedure for the depth camera is reported in Section 4. In Section 5, the test uncertainty evaluation results are discussed. Section 6 summarizes the research.

2. Test Setup

2.1. Depth Camera

In the present study, Azure Kinect (Microsoft, Redmond, WA, USA) was used. It is a sensor complex containing a depth camera and inertial measurement unit (IMU) module. The depth camera module of Azure Kinect uses ToF of infrared for measuring the distance to the object. Figure 1 shows the design of the Azure Kinect.

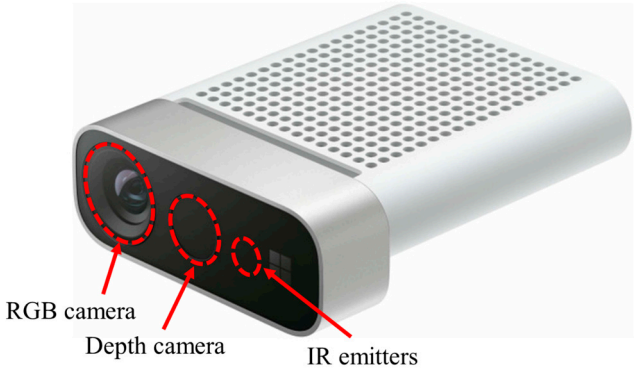

Figure 1. Configuration of optic sensors of Azure Kinect.

The IMU of Azure Kinect was used to align the sensor to be perpendicular to the calm water surface. The IMU detected 3D acceleration; thus, it could sense the direction of gravity, where the acceleration is recorded as 9.8 m/s^2 in a stationary condition. The measurement uncertainty of the IMU concerned the alignment of the depth camera system. Such uncertainty was reflected in the mapping function of calibration; thus, the uncertainty of the IMU sensor was not treated as the elemental error source in the present study.

The depth camera module is an array of infrared ToF sensors [47]. The sensor measures the time that infrared emitted from the sensor returns after reflection on the object; after multiplying by the speed of light, the travel distance of the emitted infrared beam is derived. It is noteworthy that the depth measurement is not continuous like capacitance-type and servo-needle-type wave height gauges; the maximum repetition rate of the sensor is 30 Hz. The spatial resolution of the sensor is generally 1024 × 1024 pixels, though it differs depending on the operating conditions.

The optical setup of the depth camera is presented in Table 1. In the present study, a narrow field of view (FoV) and the binned setting were used, which provide minimum distortion and noise. For the binned setup, the depth signal of a pixel is compared with that of neighbor pixels to increase the reliability of the measurement. Therefore, the effective spatial resolution reduces, but the noise in the measurement is significantly suppressed [43,48].

Table 1. Optical setup of Azure Kinect [49].

Mode	Resolution (Pixels)	Field of Interest (°)	Frame-Per-Second (Hz)	Operating Range (m)	Exposure Time (ms)
Narrow FoV—unbinned	640 × 576	75 × 65	0, 5, 15, 30	0.5–3.86	12.8
Narrow FoV—2 × 2 binned	320 × 288	75 × 65	0, 5, 15, 30	0.5–5.46	12.8
Wide FoV—2 × 2 binned	512 × 512	120 × 120	0, 5, 15, 30	0.25–2.88	12.8
Wide FoV—unbinned	1024 × 1024	120 × 120	0, 5, 15	0.25–2.21	20.3
Passive IR	1024 × 1024	Not applicable	0, 5, 15, 30	N/A	1.6

2.2. Wave Flume

Wave elevation field measurement was conducted in the wave flume of Chungnam National University. Its length and width are 18 m and 1.2 m, respectively. The maximum depth of the flume is 1 m, but the depth was set as 0.7 m for the present study. Figure 2 shows the test arrangement. Azure Kinect was located 600 mm above the calm water surface. Ultrasonic and capacitance-type wave height gauges were installed near the FoV of the depth camera.

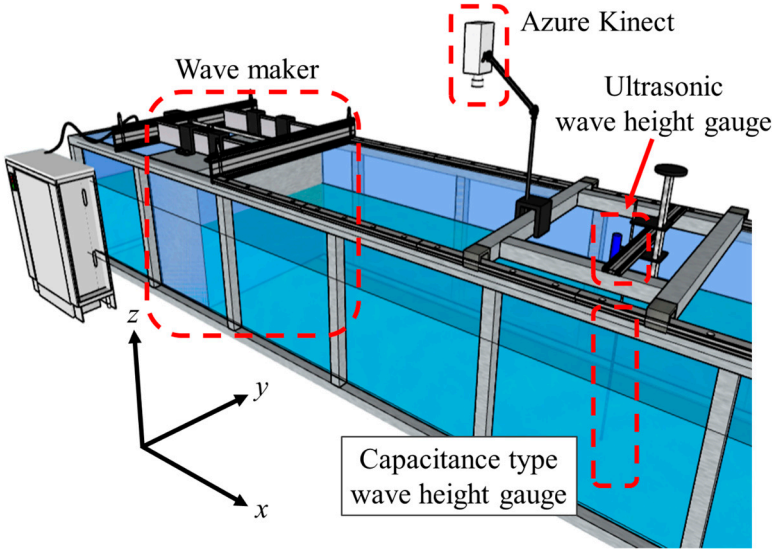

Figure 2. Test arrangement of wave elevation field measurement in the wave flume.

The piston-type wavemaker at the end of the flume generated regular wave trains by controlling the stroke and period (T) of the piston motion. The period of the wavemaker ranged from 0.35 s to 1.35 s. The generated wave was also measured using an AWP-24-2 capacitance-type wave height gauge (Akamina Technologies, Ottawa, Canada) and P49 ultrasonic wave height gauge (PIL Sensoren GmbH, Erlensee, Germany). The repetition rate of both wave height gauges was 30 Hz, to be the same as that of the depth camera. Measurement results for different wave height gauges were compared with the assessed test uncertainty in the study.

For ToF measurement, the water surface should reflect the infrared; however, water absorbs infrared rather than reflects it. To enhance the reflectivity, dyes and tracer particles were used in previous studies [42,43]. Considering that the test is performed in a wave flume, the required volume of dye would be excessive, although water-soluble paint showed good performance in the depth camera operation of Toselli et al. [42]. In the present study, a fine tracer particle that floats on the water surface and blocks infrared was used to replace water-soluble paint. Considering the price and required amount of tracer particles, pine pollen was selected. It is an organic material that does not pollute the drained water.

2.3. Test Cases

Figure 3 shows the test condition. The test condition was mainly determined based on the wave stiffness (H/λ), as wave height gauges of ToF types have weak power to measure large stiffness, for which they lose the reflected signal. The wave height (H) in Figure 3 was estimated from the analytic solution of the moving plate in water [50]. The wavelength (λ) was computed from the dispersion relationship of the water wave,

$$\left(\frac{2\pi}{T}\right)^2 = gk\tanh(kD) \quad (1)$$

where D, g, and k are the depth of the flume, gravitational acceleration, and wave number ($k = 2\pi/\lambda$), respectively. H/λ ranged from 1/100 to 1/12.5 in a scenario where the infinite depth condition, i.e., $\lambda > 2D$, is not maintained for λ in some long periods, i.e., $T > 0.94$ s.

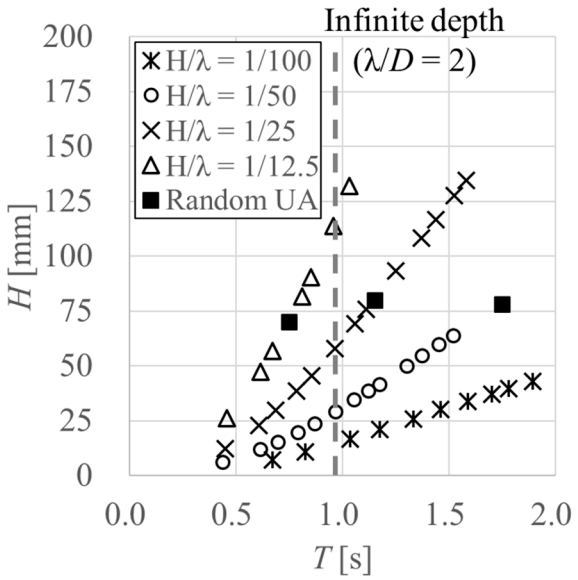

Figure 3. Test condition for wave measurement. Random UA, test cases for random standard uncertainty assessment.

For all test conditions, the wave elevation was measured using the depth camera and capacitance-type wave height gauge. Measurement results for the capacitance-type wave height gauge are regarded as the reference. Therefore, the reference wave amplitude (A_W) is defined as half of the wave height measured by the capacitance-type wave height gauge, rather than the analytic solution.

Tests indicated as solid squares in Figure 3 were repeated five times for random standard uncertainty assessment in the three conditions with wave stiffness variation ($H/\lambda = 1/12.5, 1/25, 1/50$). Measurements of the ultrasonic-type wave height gauge were added for the random standard uncertainty assessment test cases. For other conditions, tests were performed one time and the trends of measurements were compared between the capacitance-type wave height gauge and depth camera.

3. Principles of Test Uncertainty Assessment

In the present study, the test uncertainty of wave elevation measurement at a certain point, ζ (x, y), was evaluated based on the American Society of Mechanical Engineers (ASME) standard [51]. This section explains the procedure for estimating the combined standard uncertainty of wave elevation measurement, u_ζ. The time series of wave elevation measured by a wave height gauge is a set of instantaneous measurements rather than the time-mean of measurements; thus, it should be treated as a single measurement. The test uncertainty assessment aims to derive the confidence interval in which the true value is expected to be placed with a certain probability. For a typical test uncertainty assessment, a confidence interval of 95% is assessed.

To introduce the test uncertainty, the concept of error should be clarified. The total error is the difference between the true value and single test results. The total error can be divided into two elements: random error and systematic error. Like the composition of two error elements, it is assumed that the combined standard uncertainty consists of the random (s_ζ) and systematic standard uncertainty (b_ζ). That is obtained by calculating the root-sum-square of two uncertainty elements, as shown in Equation (2), while the total error is a simple sum of the random error and systematic error.

$$u_\zeta = \sqrt{(b_\zeta)^2 + (s_\zeta)^2} \quad (2)$$

The random error correlates with the repeatability of the tests. If the test is repeated infinitely, the population mean of the test results can be obtained, and the random error

is defined as the difference between the population mean and a single test result. The expected level of random error is defined as the random standard uncertainty. By repeating tests of finite numbers, the sample mean and sample standard deviation, $\overline{\zeta}$ and s_ζ, can be obtained as follows,

$$\overline{\zeta} = \frac{\sum \zeta_j}{N} \tag{3}$$

$$s_{\zeta 1} = \sqrt{\sum \frac{\left(\zeta_j - \overline{\zeta}\right)^2}{N-1}} \tag{4}$$

where N is the number of measurements. The random standard deviation of the sample mean, $s_{\zeta 2}$, considers the uncertainty of estimation of the population mean from the sample mean. It is derived as follows,

$$s_{\zeta 2} = \frac{s_{\zeta 1}}{\sqrt{N}} \tag{5}$$

Following Student's t-distribution, the estimation of the true population mean with a 95% confidence level is obtained as $\overline{\zeta} \pm t_{95} s_{\zeta 2}$. The random standard uncertainty of ζ measurement is derived from $s_{\zeta 1}$ and $s_{\zeta 2}$, as shown in Equation (6).

$$s_\zeta = \sqrt{\left(s_{\zeta 1}\right)^2 + \left(s_{\zeta 2}\right)^2} = \sqrt{\sum \frac{\left(\zeta_j - \overline{\zeta}\right)^2}{N-1} + \sum \frac{\left(\zeta_j - \overline{\zeta}\right)^2}{(N-1)N}} \tag{6}$$

The systematic error is the difference between the population mean and true value. As the true value is not known in most cases, only the expected level of the systematic error, i.e., the systematic standard uncertainty, is available, rather than the specific systematic error value. The systematic standard uncertainty of the measurement is established from the systematic standard uncertainty of elements (b_k) and its sensitivity (θ_k), as follows,

$$b_{\overline{\zeta}} = \left[\sum \left(b_{\overline{\zeta}_k}\right)^2\right]^{\frac{1}{2}} = \left[\sum \left(\theta_k b_k\right)^2\right]^{\frac{1}{2}} \tag{7}$$

4. Calibration Procedure

Figure 4 shows the procedure of wave height measurement using the depth camera. The error propagation for systematic uncertainty assessment follows the procedure. The system output is the wave elevation field, (x, y, ζ). The depth camera provides the point cloud of pixel-wise location and measured depth (X, Y, h). The correspondence between (X, Y, h) and (x, y, ζ) should be identified by calibration.

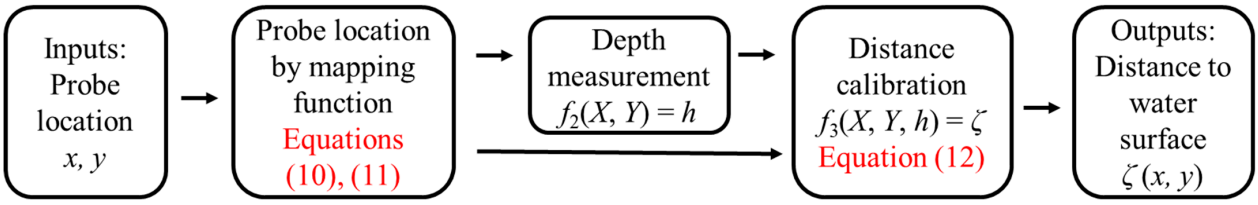

Figure 4. Procedure for measuring wave elevation field using the depth camera.

The measurement is separated into three steps: finding a pixel-wise location corresponding to the physical location, i.e., $f_1(x, y) = (X, Y)$, reading the depth at the pixel-wise location from the instantaneous point cloud data, i.e., $f_2(X, Y) = h$, and converting h to ζ, i.e., $f_3(X, Y, h) = \zeta$. Knowing that f_2 is a simple data reading, f_1 and f_3 require calibration before measurement.

The mapping function $f_1(X, Y) = (x, y)$ is established based on the calibration of particle image velocimetry, which acquires the velocity field of a plane from pixel images [52]. For two-dimensional (2D) imaging without distortion, the pixel and physical location linearly correlate to each other; thus, the calibration from (x, y) and (X, Y) can be derived as follows,

$$X = \alpha x \tag{8}$$

$$Y = \beta y \tag{9}$$

The depth camera of Azure Kinect has barrel distortion of the image, and a simple linear mapping function is applicable, as set out in Equations (8) and (9) and as shown in Figure 4. A mapping function of polynomial form can be used to correct the distorted image [53]. In the present study, the third-order polynomial of X and Y was used, as follows,

$$x = \alpha_{30}X^3 + \alpha_{21}X^2Y + \alpha_{20}X^2 + \alpha_{12}XY^2 + \alpha_{11}XY + \alpha_{10}X + \alpha_{03}Y^3 + \alpha_{02}Y^2 + \alpha_{01}Y + \alpha_{00} \tag{10}$$

$$Y = \beta_{30}X^3 + \beta_{21}X^2Y + \beta_{20}X^2 + \beta_{12}XY^2 + \beta_{11}XY + \beta_{10}X + \beta_{03}Y^3 + \beta_{02}Y^2 + \beta_{01}Y + \beta_{00} \tag{11}$$

The calibration target shown in Figure 5 was used for establishing the mapping function. The embossed markers on a flat optic table were captured by the depth camera. The height of the marker and the physical distance between embossed markers were 15 mm and 50 mm, respectively. Based on the datasets of (x, y) and (X, Y) of 25 markers on the calibration target, third-order polynomial mapping functions of Equations (10) and (11) were derived using a Python-based custom program. The program was developed using Scikit-learn, a machine-learning library.

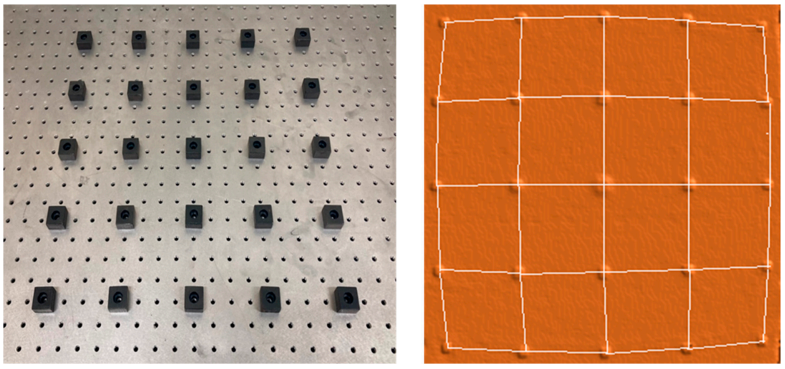

Figure 5. Calibration target (**left**) and depth image of the target with barrel distortion (**right**).

The calibration function of ζ and h (f_3 in Figure 4) was acquired by measuring h to the calm water surface, using the depth camera, with a known distance. The same calibration method was also applied to the capacitance and ultrasonic wave height gauges. Figure 6 shows a schematic of the distance calibration, f_3. The depth camera was vertically traversed using a lead screw from 700 mm to 550 mm. The resolution of the vertical position adjustment was 1 mm.

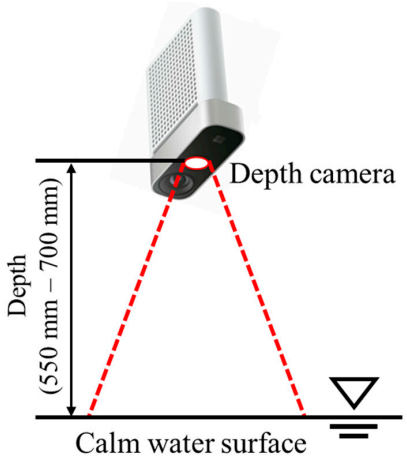

Figure 6. Depth calibration of depth camera on the calm water surface.

The depth calibration function f_3 was established assuming linearity, as shown in Equation (12). Figure 7 shows calibration results. Twelve points on the depth image were selected for depth calibration, as shown in Figure 7a, to compare h and ζ. Figure 7b shows the correlation between h and ζ with (X, Y) locations on the image. As ζ was independent of X, γ_1 in Equation (12) was determined to be zero, but Y showed a strong correlation with ζ. The relationship between h and ζ-to-Y location variation was established as Equations (13)–(16).

$$\zeta = f_3(X, Y, h) = (\gamma_1 X + \gamma_2 Y + \gamma_3)h \tag{12}$$

$$(Y = 60) : \zeta = 1.0559h - 3.802 \tag{13}$$

$$(Y = 120) : \zeta = 1.0159h - 0.718 \tag{14}$$

$$(Y = 180) : \zeta = 0.9787h + 2.931 \tag{15}$$

$$(Y = 240) : \zeta = 0.9536h - 2.061 \tag{16}$$

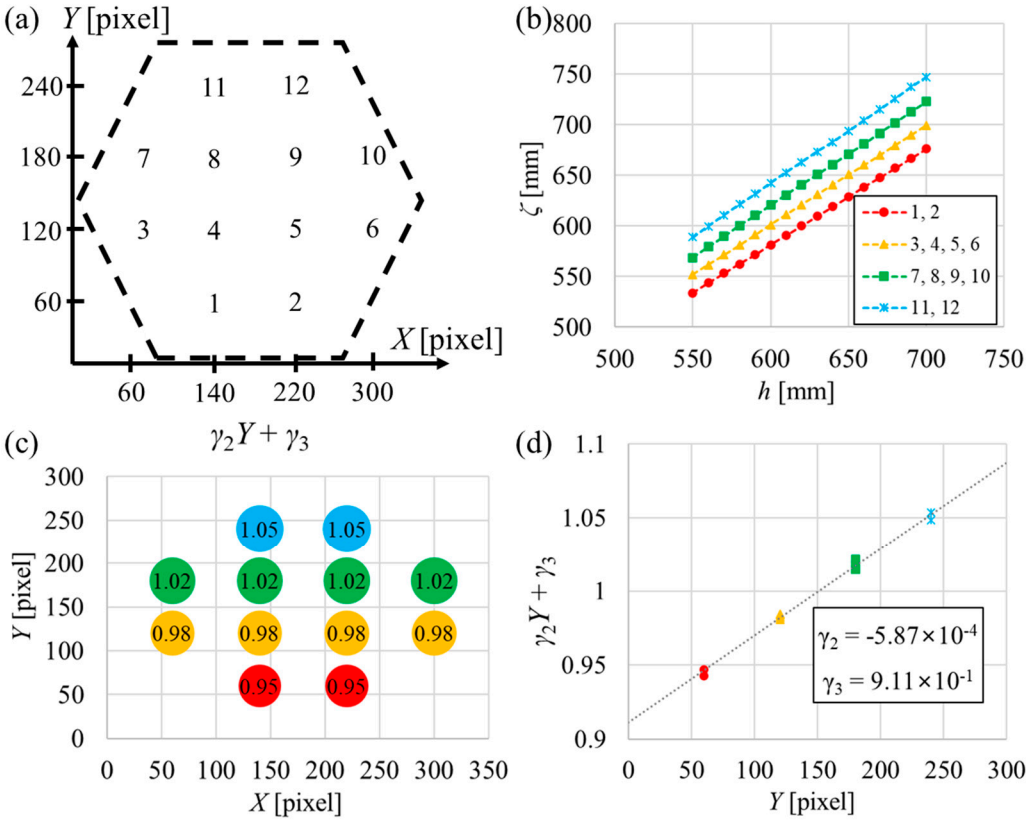

Figure 7. Distance calibration procedure and results: (**a**) pixel locations of depth calibration probes, (**b**) depth measurement results, (**c**) slope ($\gamma_2 Y + \gamma_3$) by pixel-wise locations, (**d**) determination of γ_2 and γ_3.

Figure 7c shows the slope ($\gamma_2 Y + \gamma_3$) of Equations (13)–(16) concerning Y variation. As shown in Figure 7d, γ_2 and γ_3 were determined to be -5.87×10^{-4} and 0.911, respectively. The coefficients of Equations (10)–(12) by calibration are presented in Table 2.

Table 2. Calibration results.

$f_1(X, Y) = x$		$f_1(X, Y) = y$		$f_3(X, Y, h) = \zeta$	
α_{30}	2.10×10^{-1}	β_{30}	4.48×10^{-2}	γ_1	0
α_{21}	-1.87×10^{-3}	β_{21}	1.61×10^{-5}	γ_2	-5.87×10^{-4}
α_{20}	2.77×10^{-6}	β_{20}	2.92×10^{-4}	γ_3	9.1×10^{-1}
α_{12}	2.10×10^{-5}	β_{12}	9.37×10^{-7}		
α_{11}	-1.75×10^{-3}	β_{11}	-2.21×10^{-3}		
α_{10}	1.94×10^{-5}	β_{10}	-7.49×10^{-6}		
α_{03}	-3.94×10^{-3}	β_{03}	1.68×10^{-5}		
α_{02}	-3.33×10^{-1}	β_{02}	-3.71×10^{-3}		
α_{01}	2.94	β_{01}	3.01		
α_{00}	0	β_{00}	0		

5. Test Uncertainty Assessment

As discussed in Section 4, two calibrations to acquire f_1 and f_3 were applied to the wave elevation field measurement using the depth camera. The systematic standard uncertainties of the elemental error sources, i.e., probe location (b_x, b_y), resolution of depth measurement (b_{f2}), and uncertainty of the depth calibration (b_{f3}), were propagated along the data process and constituted b_ζ, as follows,

$$b_\zeta = \sqrt{\left(\theta_{f1}\sqrt{{b_x}^2 + {b_y}^2}\right)^2 + \left(\theta_{f3}\sqrt{b_{f2}^2 + b_{f3}^2}\right)^2} \quad (17)$$

If the physical location of the probe was given, the corresponding location on the depth image was determined by the mapping functions of Equations (10) and (11). The standard deviations of errors of the physical location and reconstructed location by the mapping function in the x- and y-directions were defined as b_x and b_y, respectively.

To quantify the reconstruction error, embossed markers for the calibration were rearranged into 3×3 and 4×4. The marker locations were acquired from the depth image and compared with the physical ones. Figure 8 shows a comparison of actual and reconstructed marker locations. The standard deviations of the error, i.e., b_x and b_y, were 2.2 mm and 3.4 mm, respectively.

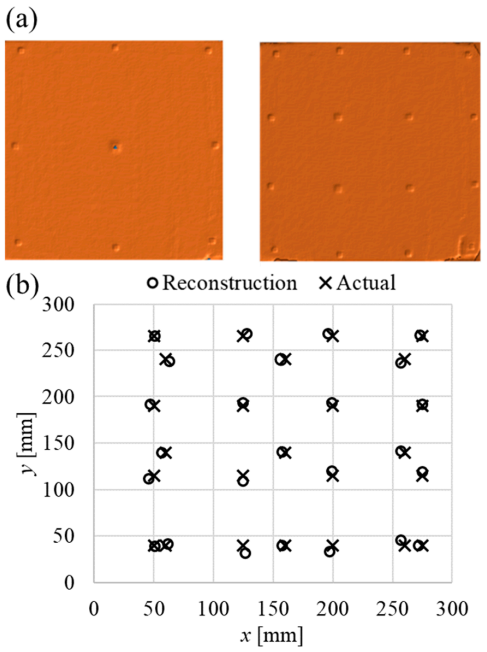

Figure 8. Reconstruction of locations of the markers: (**a**) depth image of 3×3 and 4×4 arrangements, (**b**) comparison of actual and reconstructed locations.

The sensitivity, θ_{f1}, was derived from $\partial\zeta/\partial x$ and $\partial\zeta/\partial y$. This could be interpreted as the wave slope at the probe point. If the wave was approximated in a sinusoidal function of Equation (18), the mean wave slope or θ_{f1} could be expressed as the function of H/λ, as shown in Equation (19). For capacitance-type and ultrasonic wave height gauge measurements, the systematic standard uncertainties for locating capacitance-type and ultrasonic gauges were suggested to be 2 mm and 5 mm, respectively, by the generic test environment.

$$\zeta(x) = A_w \sin kx \tag{18}$$

$$\theta_{f1} = \overline{\frac{\partial\zeta}{\partial x}} = \frac{1}{\lambda}\int_0^\lambda \left|\frac{\partial\zeta}{\partial x}\right| dx = \frac{1}{\lambda}\int_0^\lambda |kA_w \cos kx| dx = \frac{2H}{\lambda} \tag{19}$$

To estimate b_{f2}, the resolution of the depth measurement should be considered as 1 mm. If the measured depth is expressed as h, the actual measurement is expected to range as in Equation (20). For a 95% confidence level, t = 2 and b_{f2} = 0.25 mm.

$$h \pm 0.5mm = h \pm t_{95} b_{f2} \tag{20}$$

The systematic standard uncertainty of depth calibration, b_{f3}, was evaluated from the calibration data of Figure 7b. Similar to b_{f1}, the standard deviation of the error of the actual calibration point and reconstructed value by the calibration function f_3 was defined as b_{f3}. Both b_{f2} and b_{f3} concern h and ζ, and they share the same sensitivity of θ_{f3}. θ_{f3} is the sensitivity of h to ζ, i.e., $\partial\zeta/\partial h$ was obtained from Equations (13)–(16). The mean of θ_{f2} in Equations (13)–(16) was 1.00. For systematic standard uncertainty of the capacitance-type and ultrasonic wave height gauges, b_{f3} was assessed in the same manner as the depth camera case, as the calibration of f_3 was performed. Table 3 summarizes the systematic standard uncertainty assessment results for three wave height sensors.

Table 3. Systematic standard uncertainty assessment results.

	Wave Condition H/λ	Probe Location (f_1)			Depth Measurement (f_2)	Depth Calibration (f_3)		Systematic Standard Uncertainty b_ζ (mm)
		θ_{f1}	b_X (mm)	b_Y (mm)	b_{f2} (mm)	θ_{f3}	b_{f3} (mm)	
Depth camera	1/12.5	0.16	2.2	3.4	0.25	1.00	0.32	0.76
	1/25	0.08						0.52
	1/50	0.04						0.44
Capacitance-type wave height gauge	1/12.5	0.16	2	2	-	1.00	0.21	0.50
	1/25	0.08						0.31
	1/50	0.04						0.24
Ultrasonic wave height gauge	1/12.5	0.16	5	5	-	1.00	0.51	1.24
	1/25	0.08						0.76
	1/50	0.04						0.58

Figure 9 shows the time-series and fast Fourier transform (FFT) analysis results of ζ in the random standard uncertainty assessment cases indicated in Figure 3. In a large wave stiffness condition, the waveform was characterized by high-order Stokes waves, where the harmonic components raised the wave trough. It is noteworthy that the ultrasonic wave height gauge lost signal at a H/λ of 1/12.5, while the depth camera maintained the ability to measure wave elevation. The ToF sensors, i.e., a depth camera and ultrasonic wave height gauge, showed a delay of measurement when there was a descending free surface, which increased in larger wave stiffness conditions. The ToF sensors have a large measurement area for one data point, which may have disadvantages when measuring stiff surfaces, where the wave height rapidly changes in FoV. In the smallest wave stiffness condition (H/λ = 1/50), the measurement signal of the depth camera wiggled, but it was regarded as high-frequency noise that could be filtered in practical tests.

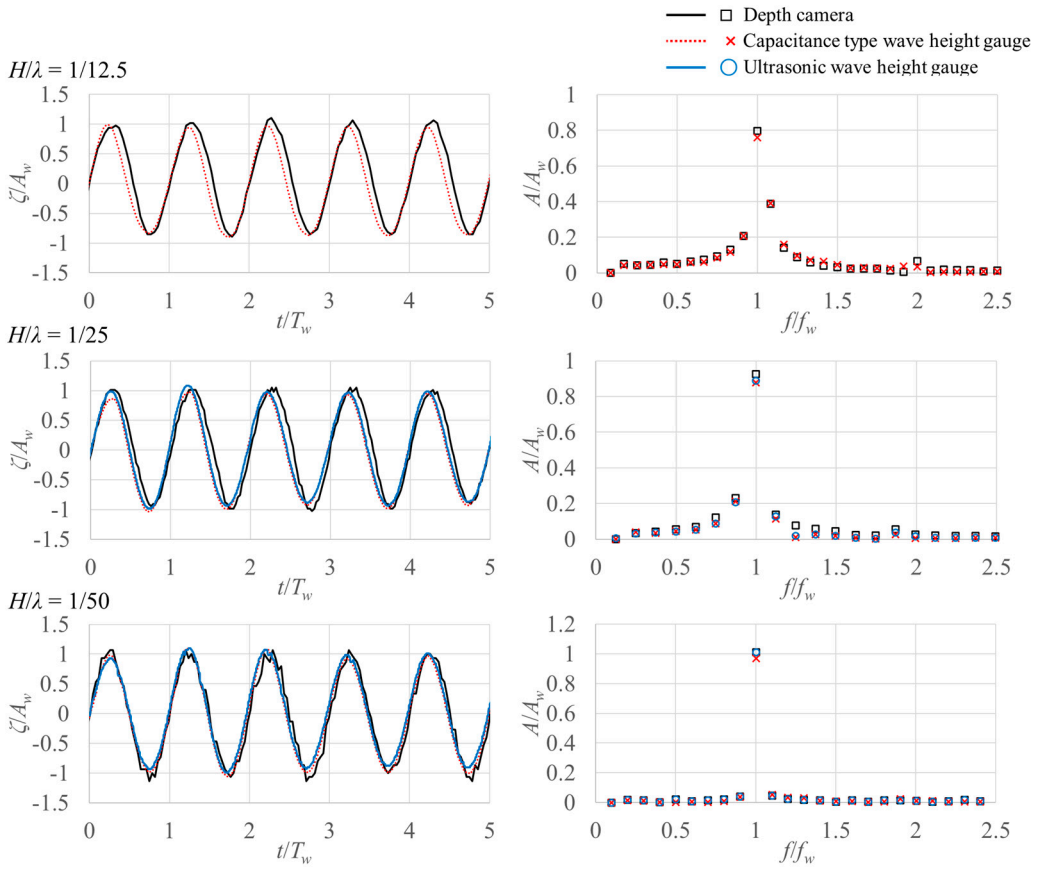

Figure 9. Wave measurement results of three wave elevation measurement systems in time and frequency domains with wave stiffness variation.

The random standard uncertainty was assessed from the standard deviation of peak magnitudes of FFT results from five repeats. In addition, the uncertainty of estimation of the population mean in Equation (5) was also considered. Table 4 shows the random standard, combined standard, and expanded uncertainty with a 95% confidence interval ($U_{\zeta 95}$) of the depth camera and two wave height gauges. $U_{\zeta 95}$ was defined via Equation (21). $t_{95} = 2.776$ was derived from Student's t-distribution for a 95% confidence interval with four degrees of freedom, as the tests were repeated five times.

$$U_{\zeta 95} = t_{95} u_{\zeta} \tag{21}$$

Table 4. Random standard, combined standard, and expanded uncertainty assessment results.

	H/λ	H (mm)	$s_{\zeta 1}$ (mm)	$s_{\zeta 2}$ (mm)	s_{ζ} (mm)	u_{ζ} (mm)	$U_{\zeta 95}$ (mm) ($U_{\zeta 95}/H$)
Depth camera	1/12.5	70	1.01	0.20	1.03	1.28	3.56 (5.1%)
	1/25	80	0.72	0.14	0.73	0.90	2.50 (3.1%)
	1/50	78	0.805	0.16	0.82	0.93	2.58 (3.3%)
Capacitance-type wave height gauge	1/12.5	70	0.695	0.14	0.71	0.87	2.41 (3.4%)
	1/25	80	0.575	0.12	0.59	0.66	1.84 (2.3%)
	1/50	78	0.465	0.09	0.47	0.53	1.47 (1.9%)
Ultrasonic wave height gauge	1/12.5	70				-	
	1/25	80	0.87	0.17	0.89	1.17	3.25 (4.1%)
	1/50	78	0.655	0.13	0.67	0.89	2.46 (3.2%)

The capacitance-type wave height gauge had the smallest test uncertainty. Among the two ToF sensors, the expanded test uncertainty of the ultrasonic wave height gauge was larger than that of the depth camera, owing to greater systematic than random standard

uncertainty from the probe location. Both random and systematic standard uncertainty enlarged along with the increase of the wave stiffness.

Figure 10 shows a comparison of the wave amplitudes at the peak frequency measured by the capacitance-type wave height gauge and depth camera. The size of the circle symbols indicates the disparity of two wave height measurements, nondimensionalized by A_W and expressed in percentage terms. Disparity was found within the expanded uncertainty range of the two sensors presented in Table 4. In general, the disparity was minimized in $H/\lambda = 1/50$, showing the best correlation between the two sensors. The correlation between the measurement results of the two sensors was mostly affected by the wave stiffness, rather than wave height variation. As presented in Table 4, the disparity increased in large wave stiffness conditions, especially for small H.

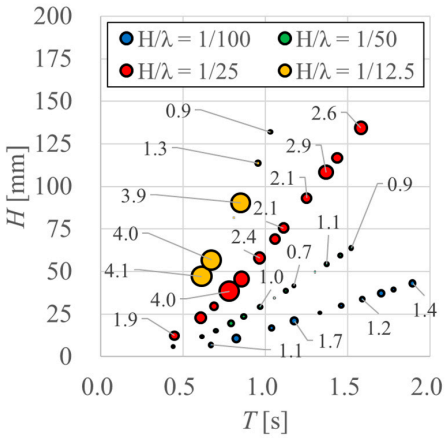

Figure 10. Comparison of peak amplitudes measured by the capacitance-type wave height gauge and depth camera.

6. Conclusions

The wave elevation field measurement procedure using a depth camera is suggested with test uncertainty assessment. Two calibration stages are suggested for the correction of distorted depth with a polynomial mapping function and depth calibration. The test uncertainty from the spatial correction was smaller than that from the depth calibration and measurement resolution.

Total test uncertainties of capacitance-type and ultrasonic wave height gauges were also evaluated in the same way with the depth camera for comparison. After calibration, regular wave fields with the wave amplitude and period variation were measured. The capacitance-type wave height gauge showed the smallest test uncertainty; thus, it was used as the reference. The systematic standard uncertainty of the depth camera was smaller than that of other ToF sensors, i.e., the ultrasonic wave height gauge.

The random standard uncertainty was assessed by repeating wave amplitude measurements but with wave stiffness variation. The magnitude of the random standard uncertainty of the depth camera was comparable to the systematic standard uncertainty. Both uncertainties increased in large wave stiffness conditions for three wave height gauges. The depth camera maintained a measurement capability for the wave stiffness of 1/12.5, while the ultrasonic wave height gauge suffered loss of measurement signal.

Through test uncertainty assessment, it was confirmed that the depth camera has a test uncertainty comparable to existing pointwise wave height gauges, while it can also measure the wave height field. The wave height field measurement can be applied to laboratory-scale experiments and actual sea conditions for efficient measurement.

Author Contributions: Conceptualization, J.S. and H.K.; methodology, J.S. and H.K.; software, H.K. and C.J.; validation, K.K.; writing—original draft preparation, H.K.; writing—review and editing, J.S.; visualization, K.K.; supervision, J.S.; project administration, J.S.; funding acquisition, J.S. All authors have read and agreed to the published version of the manuscript.

Funding: This research was funded by Chungnam National University (2020–2021).

Institutional Review Board Statement: Not applicable.

Informed Consent Statement: Not applicable.

Data Availability Statement: Publicly available datasets were analyzed in this study. This data can be presented on request.

Conflicts of Interest: The authors declare no conflict of interest.

References

1. Huang, W.; Xiao, H. Numerical modeling of dynamic wave force acting on Escambia Bay Bridge deck during Hurricane Ivan. *J. Waterw. Port Coast. Ocean Eng.* **2009**, *135*, 164–175. [CrossRef]
2. Guo, A.; Fang, Q.; Bai, X.; Li, H. Hydrodynamic experiment of the wave force acting on the superstructures of coastal bridges. *J. Bridge Eng.* **2015**, *20*, 04015012. [CrossRef]
3. Azadbakht, M.; Yim, S.C. Simulation and estimation of tsunami loads on bridge superstructures. *J. Watew. Port Coast. Ocean Eng.* **2015**, *141*, 04014031. [CrossRef]
4. Yan, J.; Korobenko, A.; Deng, X.; Bazilevs, Y. Computational free-surface fluid-structure interaction with application to floating offshore wind turbines. *Comput. Fluids* **2016**, *141*, 155–174. [CrossRef]
5. Pham, T.D.; Shin, H. The effect of the second-order wave lads on drift motion of a semi-submersible floating offshore wind turbine. *J. Mar. Sci. Eng.* **2020**, *8*, 859. [CrossRef]
6. Thiagarajan, K.; Moreno, J. Wave induced effects on the hydrodynamic coefficients of an oscillating heave plate in offshore wind turbines. *J. Mar. Sci. Eng.* **2020**, *8*, 622. [CrossRef]
7. Zhao, Y.; Guan, C.; Bi, C.; Liu, H.; Cui, Y. Experimental investigations on hydrodynamic responses of a semi-submersible offshore fish farm in waves. *J. Mar. Sci. Eng.* **2019**, *7*, 238. [CrossRef]
8. Gatin, I.; Vukcevic, V.; Jasak, H.; Seo, J.; Rhee, S.H. CFD verification and validation of green sea loads. *Ocean Eng.* **2018**, *148*, 500–515. [CrossRef]
9. Azman, N.U.; Husain, M.K.A.; Zaki, N.I.M.; Soom, E.M.; Mukhlas, N.A.; Ahmad, S.Z.A.S. Structural integrity of fixed offshore platforms by incorporating wave-in-deck. *J. Mar. Sci. Eng.* **2021**, *9*, 1027. [CrossRef]
10. Jiang, C.; el Moctar, O.; Schellin, T.E. Hydrodynamic sensitivity of moored and articulated multibody offshore structures in waves. *J. Mar. Sci. Eng.* **2021**, *9*, 1028. [CrossRef]
11. Begovic, E.; Bertorello, C.; Pennino, S. Experimental seakeeping assessment of a warped planing hull model series. *Ocean Eng.* **2014**, *83*, 1–15. [CrossRef]
12. Park, D.-M.; Lee, J.; Kim, Y. Uncertainty analysis for added resistance experiment of KVLCC2 ship. *Ocean Eng.* **2015**, *95*, 143–156. [CrossRef]
13. Seo, J.; Choi, H.; Jeong, U.-C.; Lee, D.K.; Rhee, S.H.; Jung, C.-M.; Yoo, J. Model tests on resistance and seakeeping performance of wave-piercing high-speed vessel with spray rails. *Int. J. Nav. Archit. Ocean Eng.* **2016**, *8*, 442–455. [CrossRef]
14. Begovic, E.; Bertorello, C.; Pennino, S.; Piscopo, V.; Scamardella, A. Statistical analysis of planing hull motions and accelerations in irregular head sea. *Ocean Eng.* **2016**, *112*, 253–264. [CrossRef]
15. Kim, W.J.; Van, S.H.; Kim, D.H. Measurement of flows around modern commercial ship models. *Exp. Fluids* **2001**, *31*, 567–578. [CrossRef]
16. Longo, J.; Stern, F. Uncertainty assessment for towing tank tests with example for surface combatant DTMB Model 5415. *J. Ship Res.* **2005**, *49*, 55–68. [CrossRef]
17. Kashiwagi, M. Hydrodynamic study on added resistance using unsteady wave analysis. *J. Ship Res.* **2013**, *57*, 220–240.
18. Lee, D.; Hong, S.Y.; Lee, G.-J. Theoretical and experimental study on dynamic behavior of a damaged ship in waves. *Ocean Eng.* **2007**, *34*, 21–31. [CrossRef]
19. Lee, S.; You, J.-M.; Lee, H.-H.; Lim, T.; Park, S.T.; Seo, J.; Rhee, S.H.; Rhee, K.-P. Experimental study on the six degree-of-freedom motions of a damaged ship floating in regular waves. *IEEE J. Ocean. Eng.* **2016**, *41*, 40–49.
20. Espinoza Haro, M.P.; Seo, J.; Sadat-Hosseini, H.; Seok, W.-C.; Rhee, S.H.; Stern, F. Numerical simulations for the safe return to port of a damaged passenger ship in head or following seas. *Ocean Eng.* **2017**, *143*, 305–318. [CrossRef]
21. Begovic, E.; Bertorello, C.; Bove, A.; Garme, K.; Lei, X.; Persson, J.; Petrone, G.; Razola, M.; Rosen, A. Experimental modelling of local structure responses for high-speed planing craft in waves. *Ocean Eng.* **2020**, *216*, 107986. [CrossRef]
22. Tavakoli, S.; Bilandi, R.N.; Mancini, S.; De Luca, F.; Dashtimanesh, A. Dynamic of a planing hull in regular waves: Comparison of experimental, numerical and mathematical methods. *Ocean Eng.* **2020**, *217*, 107959. [CrossRef]
23. Metcalf, B.; Longo, J.; Ghosh, S.; Stern, F. Unsteady free-surface wave-induced boundary-layer separation for a surface-piercing NACA 0024 foil: Towing tank experiments. *J. Fluids Struct.* **2006**, *22*, 77–98. [CrossRef]
24. Liu, J.; Guo, A.; Li, H. Experimental investigation on three-dimensnional structures of wind wave surfaces. *Ocean Eng.* **2022**, *265*, 112628. [CrossRef]
25. Lev, S. Laboratory study of temporal and spatial evolution of waves excited on water surface initially at rest by impulsive wind forcing. *Procedia IUTAM* **2018**, *26*, 153–161.

26. Benetazzo, A.; Fedele, F.; Gallego, G.; Shih, P.C.; Yezzi, A. Offshore stereo measurements of gravity waves. *Coast. Eng.* **2012**, *64*, 127–138. [CrossRef]
27. Benetazzo, A.; Barbariol, F.; Bergamasco, F.; Torsello, A.; Carniel, S.; Sclavo, M. Observation of extreme sea waves in a space-time ensemble. *J. Phys. Oceanogr.* **2015**, *45*, 2261–2275. [CrossRef]
28. Benetazzo, A.; Barbariol, F.; Bergamasco, F.; Torsello, A.; Carniel, S.; Sclavo, M. Stereo wave imaging from moving vessels: Practical use and applications. *Coast. Eng.* **2016**, *109*, 114–127. [CrossRef]
29. van Meerkerk, M.; Poelma, C.; Westerweel, J. Scanning stereo-PLIF method for free surface measurements in large 3D domains. *Exp. Fluids* **2020**, *61*, 19. [CrossRef]
30. Gomit, G.; Chatellier, L.; David, L. Free-surface flow measurements by non-intrusive methods: A survey. *Exp. Fluids* **2022**, *63*, 94. [CrossRef]
31. Zarruk, G.A. Measurement of free surface deformation in PIV images. *Meas. Sci. Technol.* **2005**, *16*, 1970–1975. [CrossRef]
32. Chatellier, L.; Jarny, S.; Gibouin, F.; David, L. A parametric PIV/DIC method for the measurement of free surface flows. *Exp. Fluids* **2013**, *54*, 1488. [CrossRef]
33. Caplier, C.; Rousseaux, G.; Calluaud, D.; David, L. Energy distribution in shallow water ship wakes from a spectral analysis of the wave field. *Phys. Fluids* **2016**, *28*, 107104. [CrossRef]
34. Tsubaki, R.; Fujita, I. Stereoscopic measurement of a fluctuating free surface with discontinuities. *Meas. Sci. Technol.* **2005**, *16*, 1894–1902. [CrossRef]
35. Evers, F.M. Videometric water surface tracking of spatial impulse wave propagation. *J. Vis.* **2018**, *21*, 903–907. [CrossRef]
36. Gomit, G.; Chatellier, L.; Calluaud, D.; David, L.; Frechou, D.; Boucheron, R.; Perelman, O.; Hubert, C. Large-scale free surface measurement for the analysis of ship waves in a towing tank. *Exp. Fluids* **2015**, *56*, 184. [CrossRef]
37. Sanada, Y.; Toda, Y.; Hamachi, S. Free surface measurement by reflected light image. In Proceedings of the 25th International Towing Tank Conference, Fukuoka, Japan, 14–20 September 2008.
38. Jähne, B.; Schmidt, M.; Rocholz, R. Combined optical slope/height measurements of short wind waves: Principle and calibration. *Meas. Sci. Technol.* **2005**, *16*, 1937–1944. [CrossRef]
39. Zappa, C.J.; Banner, M.L.; Schultz, H.; Corrada-Emmanuel, A.; Wolff, L.B.; Yalcin, J. Retrieval of short ocean wave slope using polarimetric imaging. *Meas. Sci. Technol.* **2008**, *19*, 055503. [CrossRef]
40. Park, H.S.; Sim, J.S.; Yoo, J.; Lee, D.Y. The breaking wave measurement using terrestrial LIDAR: Validation with field experiment on the Mallipo Beach. *J. Coast. Res.* **2011**, *64*, 1718–1721.
41. Deems, J.S.; Painter, T.H.; Finnegan, D.C. Lidar measurement of snow depth: A review. *J. Glaciol.* **2013**, *59*, 467–479. [CrossRef]
42. Toselli, F.; De Lillo, F.; Onorato, M.; Boffetta, G. Measuring surface gravity waves using a Kinect sensor. *Eur. J. Mech. B Fluids* **2019**, *74*, 260–264. [CrossRef]
43. Kim, H.; Jeon, C.; Seo, J. Development of wave height field measurement system using a depth camera. *J. Soc. Nav. Archit. Korea* **2021**, *58*, 382–390. (In Korean) [CrossRef]
44. Sciacchitano, A.; Wieneke, B. PIV uncertainty propagation. *Meas. Sci. Technol.* **2016**, *27*, 084006. [CrossRef]
45. Han, B.W.; Seo, J.; Lee, S.J.; Seol, D.M.; Rhee, S.H. Uncertainty assessment for a towed underwater stereo PIV system by uniform flow measurement. *Int. J. Nav. Archit. Ocean Eng.* **2018**, *10*, 596–608. [CrossRef]
46. Sciacchitano, A. Uncertainty quantification in particle image velocimetry. *Meas. Sci. Technol.* **2019**, *30*, 092001. [CrossRef]
47. Bamji, C.S.; Mehta, S.; Thompson, B.; Elkhatib, T.; Wurster, S.; Akkaya, O.; Payne, A.; Godbaz, J.; Fenton, M.; Rajasekaran, V.; et al. IMpixel 65nm BSI 320MHz demodulated TOF Image sensor with 3µm global shutter pixels and analog binning. In Proceedings of the 2018 IEEE International Solid—State Circuits Conference—(ISSCC), San Francisco, CA, USA, 11–15 February 2018.
48. Tölgyessy, M.; Dekan, M.; Chovanec, Ľ.; Hubinský, P. Evaluation of the Azure Kinect and its comparison to Kinect V1 and Kinect V2. *Sensors* **2021**, *21*, 413. [CrossRef] [PubMed]
49. Microsoft Corporation. *Microsoft Docs—Azure Kinect DK Documentation: Azure Kinect DK Hardware Specification*; Microsoft Corporation: Redmond, WA, USA, 2021.
50. Kim, H.; Oh, J.; Lew, J.; Rhee, S.H.; Kim, J.H. Wave and wave board motion of hybrid wave maker. *J. Soc. Nav. Archit. Korea* **2021**, *58*, 339–347. (In Korean) [CrossRef]
51. *ASME PTC 19.1-2005*; Test Uncertainty. American Society of Mechanical Engineers (ASME): New York, NY, USA, 2005.
52. Prasad, A.K. Stereoscopic particle image velocimetry. *Exp. Fluids* **2000**, *29*, 103–116. [CrossRef]
53. Soloff, S.M.; Adrian, R.J.; Liu, Z.-C. Distortion compensation for generalized stereoscopic particle image velocimetry. *Meas. Sci. Technol.* **1997**, *8*, 1441–1454. [CrossRef]

Disclaimer/Publisher's Note: The statements, opinions and data contained in all publications are solely those of the individual author(s) and contributor(s) and not of MDPI and/or the editor(s). MDPI and/or the editor(s) disclaim responsibility for any injury to people or property resulting from any ideas, methods, instructions or products referred to in the content.